JGR Oceans

RESEARCH ARTICLE

Key Points:
- Shelf-edge upwelling occurs over the North Kenya Banks (NKB) during the Northeast Monsoon, leading to higher productivity
- Strong events can occur and exhibit considerable interannual variability in intensity, position, and spatial extent
- The Somali-Zanzibar Confluence Zone exerts an important control on the upwelling, which is enhanced when it is positioned further south

Correspondence to:
Z. L. Jacobs,
zoe.jacobs@noc.ac.uk

Shelf-Break Upwelling and Productivity Over the North Kenya Banks: The Importance of Large-Scale Ocean Dynamics

Z. L. Jacobs[1], F. Jebri[1], D. E. Raitsos[2,3], E. Popova[1], M. Srokosz[1], S. C. Painter[1], F. Nencioli[2], M. Roberts[1,4], J. Kamau[5], M. Palmer[1], and J. Wihsgott[1]

[1]National Oceanography Centre, Southampton, UK, [2]Plymouth Marine Laboratory, Plymouth, UK, [3]National and Kapodistrian University of Athens, Athens, Greece, [4]Nelson Mandela University, Ocean Sciences Campus, Port Elizabeth, South Africa, [5]Kenya Marine and Fisheries Institute, Mombasa, Kenya

Abstract The North Kenya Banks (NKBs) have recently emerged as a new frontier for food security and could become an economically important fishery for Kenya with improved resources providing better accessibility. Little research has been done on the mechanisms supporting high fish productivity over the NKBs with information on annual and interannual environmental variability lacking. Here we use a high-resolution, global, biogeochemical ocean model with remote sensing observations to demonstrate that the ocean circulation exerts an important control on the productivity over the NKBs. During the Northeast Monsoon, which occurs from December to February, upwelling occurs along the Kenyan coast, which is topographically enhanced over the NKBs. Additionally, enhanced upwelling events, associated with widespread cool temperatures, elevated chlorophyll, nutrients, primary production, and phytoplankton biomass, can occur over this region. Eight such modeled events, characterized by primary production exceeding 1.3 g C/m^{-2}/day, were found to occur during January or February from 1993–2015. Even though the upwelling is always rooted to the NKBs, the position, spatial extent, and intensity of the upwelling exhibit considerable interannual variability. The confluence zone between the Somali Current and East African Coastal Current (referred to as the Somali-Zanzibar Confluence Zone) forms during the Northeast Monsoon and is highly variable. We present evidence that when the Somali-Zanzibar Confluence Zone is positioned further south, it acts to enhance shelf-edge upwelling and productivity over the NKBs. These findings provide the first indication of the environmental controls that need to be considered when developing plans for the sustainable exploitation of the NKB fishery.

Plain Language Summary The North Kenya Banks (NKBs) have recently emerged as a region capable of sustaining a rich fishery, which would boost Kenya's economy. Little research has been conducted on the environmental controls that affect these fisheries and whether there is annual variability over multiple years. Here an ocean model is used, with satellite remote sensing data, to investigate how the ocean influences this region. Specifically, the convergence of two currents during the Northeast Monsoon, the Somali Current and the East African Coastal Current, which meet near the NKBs and flow away from the coast. This induces the upwelling of cold, nutrient-rich waters, which are brought up from depth to the surface, resulting in the NKBs being a highly productive area. The confluence of these two currents forms from December to February and its position along the Kenyan coast varies from year-to-year. This leads to considerable variability in the intensity, position, and spatial extent of productive waters. Productivity is enhanced over the NKBs when the confluence of the two currents is generally positioned further south. These findings provide the first indication of the environmental controls that need to be taken into account when developing plans for sustainable exploitation of the fisheries resources.

1. Introduction

The coastal zone waters of the Western Indian Ocean (WIO) represent a pillar for livelihoods and the economic sector (Jury et al., 2010), with small-scale fisheries providing food security to the coastal East African population (Barnes-Mauthe et al., 2013). In Kenya, fisheries are mostly artisanal (FAO, 2016; Sanders et al., 1988) with an average reported annual catch (based on landing sites) of 8,406 tonnes (Le Manach et al., 2015). This is over 4 times less than that recorded for Tanzania (Bultel et al., 2015). Overexploitation in coastal zones has led to the decline of reef fish, which has shifted the focus onto the
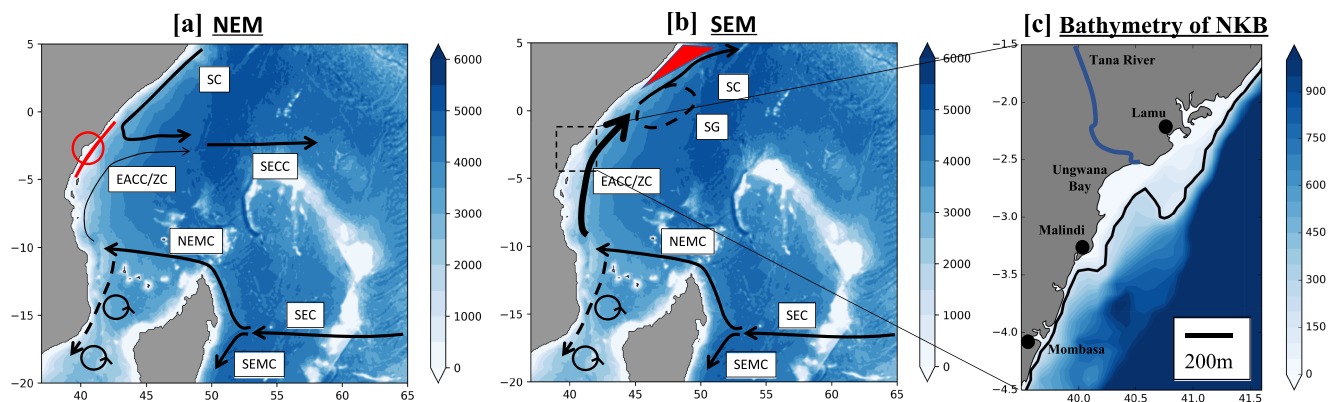
Figure 1. Bathymetry over the Western Indian Ocean (WIO) with a schematic representation of the upper ocean circulation during the Northeast Monsoon (NEM) and Southeast Monsoon (SEM)—adapted from Schott et al. (2009). The currents are the South Equatorial Current (SEC), the Southeast Madagascar Current (SEMC), the Northeast Madagascar Current (NEMC), the East African Coastal Current or Zanzibar Current (EACC/ZC), the Somali Current (SC), the Southeast Counter Current (SECC), and the Southern Gyre (SG). Red annotations indicate upwelling: (a) the red circle represents the NKB upwelling and the red lines the Ekman-induced coastal upwelling and (b) the triangle represents the Somali upwelling wedge. The thickness of the EACC/ZC represents changes in its strength. (c) Bathymetry over the NKBs is shown on the right with the 200-m isobath represented by the black line and the Tana River represented by the blue line.

pelagic fishery (Maina, 2012). This exists further offshore over the North Kenya Banks (NKBs), and is operated by a small fleet of motorized boats (Maina, 2012). The NKBs, first described by Morgans (1959), are about 45 km wide and 180 km long extending from 1.4 to 3°S and from 40.5 to 41.5°W with water depths up to 125 m (Johnson et al., 1982). The NKBs, characterized by the area inside the 200-m isobath, stand out relative to the narrow coastline of East Africa (Figure 1). As Kenya has one of the lowest marine catch rates among coastal African countries (Le Manach et al., 2015), this offshore area has been proposed as a region that could provide a boost to local fishery resources (Morgans, 1959; Wickstead, 1961). The increased utilization of motorized boats (Maina, 2012) will improve access to the NKBs, which could transform this region into an economically important fishery for the country (Akunga, 2007).

Despite this interest and potential, there is little understanding on the oceanic mechanisms that support this high fish abundance on the NKBs, in particular the annual, interannual, and multidecadal variability of the region. This is important in the context of anthropogenic climate change. A combination of economic constraints and insecurity in the region means that collecting in situ measurements in this region continues to be a major challenge (Bendeković & Vuletić, 2013). While life cycle knowledge of the species (i.e., spawning sites, migration) that make up this fishery is also scanty, it is highly likely that the dynamic ocean environment in this region will be a significant determinant of successful recruitment. Understanding this variability is therefore seen as crucial information supporting the evaluation of this emergent fishery—which would ultimately guide the development of a sustainable management plan. In this context, we now use modeling to demonstrate that the surface ocean circulation exerts an important control over the productivity of the NKBs.

The upper circulation of the WIO is subject to considerable variability associated with the East African monsoons, as outlined in Figure 1 (based on Schott et al. (2009)). The Southeast Monsoon (SEM) prevails during the austral winter (peaking in July) causing Southeasterly winds to dominate the region, while the Northeast Monsoon (NEM) Northeasterly winds prevail during the austral summer—peaking in February (Hellerman & Rosenstein, 1983; Liao et al., 2017; Mahongo et al., 2011; Ngusaru & Mohammed, 2002; Ochumba, 1983; Schott et al., 2009; Schott & McCreary, 2001). These Northeasterly winds induce upwelling along the Kenyan coast, driven by an offshore Ekman transport (e.g., Varela et al., 2015). This upwelling appears to be intensified at the NKBs with evidence of increased concentrations of nutrients at the surface and the occurrence of phytoplankton blooms (Johnson et al., 1982; Smith, 1982).

Monsoonal variability also has a clear impact on the regional (WIO) upper ocean circulation. As can be seen in Figure 1, the South Equatorial Current (SEC) flows westward across the Indian Ocean at 10–20°S all year round before branching into the Southeast Madagascar Current and the Northeast Madagascar Current (NEMC), ultimately reaching the coast of Madagascar (Schott & McCreary, 2001). The NEMC continues

toward the East African coast where it bifurcates into southward flow in the Mozambique Channel (dominated by eddies) and the northward flowing East African Coastal Current (EACC), also known as the Zanzibar Current (ZC; Fieux, 2001). The greatest speeds are observed during the SEM, exceeding 1 ms^{-1} from 4 to 5°S, and the lowest during the NEM, less than 0.3 ms^{-1} (Leetmaa et al., 1982; Swallow et al., 1991). In the shallow Zanzibar Channel, the EACC actually reverses during the NEM (Nyandwi, 2013), which is also seen in a high-resolution ocean model (Zavala-Garay et al., 2015).

During the SEM, the EACC continues northward as the Somali Current (SC) as it crosses the equator with speeds exceeding 3 ms^{-1} and a volume transport of 27 Sv in the upper 100 m (Leetmaa et al., 1982) and 74 Sv in the upper 1,000 m (Bruce, 1970). Part of the SC turns offshore at about 4°N to form a cold upwelling wedge that extends offshore from the coast while the rest re-circulates into the Southern Gyre (Schott & McCreary, 2001). During the NEM, a reversal is observed in the upper 400 m (Schott et al., 2002) with the SC now flowing southward at speeds of 0.5–1 ms^{-1} (Leetmaa et al., 1982; Molinari et al., 1990). It meets the permanently northward flowing EACC to form a confluence zone at 2–4°S, before the flow veers offshore as the eastward flowing South Equatorial Counter Current (Düing & Schott, 1978, Richardson & McKee, 1989; Shenoi et al., 1999; Schott & McCreary, 2001; Schott et al., 2009; Woodberry et al., 1989). The convergence of these two opposing currents leads to an offshore flow of the SECC to ensure continuity. Contrastingly, this offshore flow will lead to divergence at the coast. To ensure continuity of mass here, shelf-edge upwelling is likely induced over the NKBs and surrounding coastline (Kabanova, 1968; Liao et al., 2017). Specifically, this divergent flow leads to the upwelling of cold, nutrient-rich deeper waters to the surface, which is separate from localized wind-driven coastal upwelling (Varela et al., 2015), enhancing productivity over the region (e.g., Liao et al., 2017).

The Tana River discharges into Ungwana Bay (inshore of the NKBs) and is known to be one of the most productive fishing grounds along the Kenyan coast due to the influx of nutrients associated with the high sediment input (Fulanda et al., 2011; Kitheka, 2002; Mwangi, 2002). However, the Tana River outflow (and rainfall driving it) is greatest during intermonsoon periods (April–May and November) with no elevated outflow during the NEM itself (McClanahan, 1988; Tamooh et al., 2012). Furthermore, due to the high sediment outflow (and turbidity) the light levels at these shallow areas are probably very low, with the possibility of altering the local environment from a nutrient-limited to a light-limited environment (Tilstone et al., 2011). These conditions likely prevent coral ecosystems from thriving in Ungwana Bay (McClanahan & Obura, 1997; McClanahan & Young, 1996). The chlorophyll concentrations may also be influenced by the freshwater stratification from the Tana River, again altering primary productivity. This region is highly dynamic and optically complex. Seasonally varying stratification, turbidity, and flow are likely to have dramatic implications for productivity over the shelf region, including the NKBs. The local physical and biogeochemical impacts of lesser flows over similar banks have been shown to be significant (e.g., Palmer et al., 2013; Tweddle et al., 2013) with downstream biological consequences (Embling et al., 2013). Insufficient observational evidence exists, however, to assess the local impact of topographic interaction of flow over the NKBs and the high-resolution, nonhydrostatic model studies that would be required to address such processes have not, to date, been undertaken in this region.

From a research perspective, the Kenyan shelf and NKBs, in particular, are grossly undersampled with few observational campaigns over the last few decades (e.g., Roberts et al., 2008; Swallow et al., 1991) due to a combination of economic constraints and piracy along this coastline (Bendeković & Vuletić, 2013). In particular, very little work has been done on the variability of the strength or position of the confluence between the EACC/ZC and SC with only a handful of studies referring to it (e.g., Düing & Schott, 1978; Johnson et al., 1982; Schott & McCreary, 2001; Schott et al., 2002; Song et al., 2004; Mayorga-Adame et al., 2016). However, an early study using a one-layer model investigated the importance of the NKBs for the exact timing and location of the confluence zone (Johnson et al., 1982). During the NEM, they found that the NKB topography causes the eastward deflection of the EACC when the meridional flow velocity drops beneath a threshold of 0.6 ms^{-1}, in order to conserve potential vorticity. When the flow exceeds 0.6 ms^{-1} the EACC continues northward. In spite of a considerable simplification of this very complex region, the study of Johnson et al. (1982) demonstrated that the NKBs can play an important role in influencing the position of the confluence. The larger-scale wind field has also been thought to be influential in controlling the position of the confluence zone (Williams, 1963) but the topography may place a constraint on the amount of latitudinal variability if potential vorticity is conserved at low velocities (Johnson et al., 1982). In the nutrient-limited

waters of the NKBs, the likely source of nutrients during the NEM is either from upwelling (Johnson et al., 1982; Smith, 1982) or increased Tana River outflow (McClanahan, 19888).

The NKBs are located in a very complex region where a multitude of factors may be causing, or influencing the strength of, the shelf-edge upwelling over this topographic feature. Specifically, the wind field, continuity of flow (from the SECC causing divergence from the coast), and current-topography interaction could each be causing the upwelling to occur and may all be operating simultaneously. Additionally, teleconnections such as the El Niño–Southern Oscillation (ENSO), the Indian Ocean Dipole (IOD), and the Madden-Julian Oscillation (MJO) may be contributing to interannual variability of the upwelling over the NKBs.

Here, a high-resolution, global biogeochemical ocean model was used along with remote sensing observations, to synergistically investigate the importance of the position of the confluence zone on shelf-edge upwelling and productivity over the NKBs during the NEM. Previous model-based studies of this area have accurately simulated the position of the confluence zone and the eastward flow of the SECC (e.g., Pandey & Rai, 2008; Liao et al., 2017; Mayorga-Adame et al., 2016). However, even though the model domains of interest overlapped, the focus of the relative analyses was to the south of Kenya. Here the model analyses presents evidence that the position of the confluence zone is highly variable and can enhance upwelling over the NKBs when it is positioned, relatively, further south. Consequently, it exerts some control on the level of productivity in this area, while alternatively decreasing upwelling and reducing productivity when the confluence zone is positioned further north. With growing interest in the NKB ecosystem and the associated fishery it may sustain, this finding provides the first indication of the environmental controls which need to be taken into account when developing plans for future sustainable exploitation. The rest of this paper is organized as follows: methods and a description of the model and remote sensing data sets used are outlined in section 2, the results are presented (including model validation) in section 3, while the discussion and conclusions are detailed in section 4.

2. Methods

2.1. Satellite Observations

2.1.1. Ocean Color Remote Sensing

The European Space Agency Ocean Colour Climate Change Initiative (OC-CCI) has recently produced and validated one of the longest (~20 years), most complete, and consistent time series of multisensor (MODIS-Aqua, SeaWiFS, and MERIS) global satellite ocean-color data (Racault et al., 2017). The data set used in this study (v. 3.1 OC-CCI) consists of daily and monthly 1-km observations of surface chlorophyll a concentration (mg m^{-3}), from 1997 to 2017 (http://www.esa-oceancolour-cci.org/). The monthly composites were also used to calculate climatological means during the period of interest.

The remotely sensed chlorophyll observations have known limitations especially in shallow optically complex Case II waters, where suspended sediments, particulate matter, and/or dissolved organic matter do not covary in a predictable manner with chlorophyll (IOCCG, 2000). Near the coast, scattering by sediments in turbid waters (such as near the Tana River) and underwater reflectance from shallow regions may result in relatively high water-leaving radiance in the near-infrared wavelengths, which could overestimate the correction term. Despite OC-CCI using a multichlorophyll algorithm approach (see Jackson et al., 2017 for more details), remotely sensed ocean color observations over the study region may be influenced by the aforementioned factors, resulting in overestimated chlorophyll concentrations in the coastal waters and/or very shallow waters (<30 m) along the East African coast. At the same time, not all the coastal high chlorophyll values are necessarily erroneous, as the coastal regions that accommodate rivers may be sources of either nutrients or chlorophyll-rich detritus that enhance phytoplankton production near the coast (Raitsos et al., 2013). As the majority of the area included in this study comprises Case-I open waters, this bias influences only a small proportion of the data points. Furthermore, in support of the remotely sensed observations, the model outputs also show higher concentrations of chlorophyll near the coastal zone of the study area. Thus, there is evidence that the variability of the remotely sensed chlorophyll a, presented over the NKBs, is valid and not an artifact.

2.1.2. Calculation of the First Optical Depth

The first optical depth, Z90, is the penetration depth of light (e.g., Al-Naimi et al., 2017; Cherkasheva et al., 2013; Gordon & Morel, 1983). It represents how deep the satellite signal penetrates in the water column (e.g.,

Al-Naimi et al., 2017). To calculate this over the study area, the diffuse attenuation coefficient (Kd(490)) was estimated. The attenuation coefficient is commonly used to describe how visible light in the blue-green part of the spectrum is attenuated by the water column, and thus, is used as a measure for water clarity (Al-Naimi et al., 2017). The OC-CCI Kd product was computed from the inherent optical properties at 490 nm and the sun zenith angle (θ), using the Lee et al. (2005) algorithm. The first optical depth for the study area (calculated as $Z90 = 1/Kd(490)$) was on average ~17 m deep. Thus, for consistency with the satellite-derived chlorophyll observations, the model data sets were averaged over the upper 15-m depth.

2.1.3. Satellite Altimetry

Altimetry-based surface geostrophic velocities are taken from the multisatellite gridded and merged AVISO (Archiving, Validation and Interpretation of Satellite Oceanographic Data) product distributed by the Copernicus Marine Environment Monitoring Service (http://marine.copernicus.eu/services-portfolio/access-to-products/?option=com_csw&view=details&product_id=SEALEVEL_GLO_PHY_L4_REP_OBSERVATIONS_008_047). These velocities are used to assess the large-scale performance of modeled currents. The data consist of the delayed-time "Update" DUACS-DT2018 version. Geostrophic zonal and meridional velocities are computed weekly on a $1/4° \times 1/4°$ grid.

2.2. Model Configuration

Version 3.6 of the global ocean model Nucleus for European Modelling of the Ocean (NEMO; Madec, 2015), which is configured with a horizontal spatial resolution of 1/12° (Marzocchi et al., 2015; Moat et al., 2016; Webber et al., 2018), was utilized. This corresponds to about 9.25 km at the equator. The model has 75 vertical levels with finer grid spacing near the surface, that is, <1 m at the surface compared to ~250-m spacing at 5,500 m with 22 levels in the upper 100 m. The hindcast used in this study covers the time period 1958 to 2015 (56 years), with model output stored as five-day means. The bottom topography is represented as partial steps and bathymetry is derived from ETOPO2 (US Department of Commerce et al., 2006). The Louvain la Neuve (LIM2) sea-ice model is used to represent sea ice in the simulation (Timmermann et al., 2005).

The run is initialized using the World Ocean Database climatological fields (Levitus et al., 1998) and is forced by the Drakkar Surface Forcing data set version 5.2, which supplies 2-m air temperature, 2-m humidity and 10-m winds, surface radiative fluxes, and precipitation, at 0.7° horizontal resolution (Brodeau et al., 2010; Dussin et al., 2016). Sea surface salinity is relaxed toward the climatology to avoid excessive drift in global salinity. The coastal river runoff component is prescribed by a slightly adapted version of Dai and Trenbeth (2002), the details of which can be found here https://www.drakkar-ocean.eu/publications/reports/runoff-mercator-06.pdf.

The biogeochemistry is represented by MEDUSA-2, which is embedded in NEMO, and run from 1990 to 2015 (Yool et al., 2013). This is a size-based, intermediate complexity model that divides the plankton community into "small" and "large" components, and resolves the elemental cycles of nitrogen, silicon, and iron. The small component of the ecosystem is intended to represent the microbial loop of picophytoplankton and microzooplankton, while the large component covers microphytoplankton (specifically diatoms) and mesozooplankton. The nonliving particulate detritus pool is similarly split between small, slow-sinking particles that are simulated explicitly, and large, fast-sinking particles that are represented only implicitly. See Yool et al. (2013) for a full description of MEDUSA-2. Here the period 1993–2015 was used to ensure consistency between the model physics and biogeochemistry, and to avoid spin-up of the biogeochemistry component in the early 1990s. The physical and biogeochemical models have been extensively validated at the global (e.g., Popova et al., 2016; Yool et al., 2013) and regional scale, including Indian Ocean applications (e.g., Srokosz et al., 2015; Robinson et al., 2017).

3. Results

3.1. Monsoonal Variability Over the WIO (Model Validation)

To assess model performance in the WIO, we compared the modeled surface circulation with altimetric sea surface currents as shown in Figure 2. There is strong qualitative agreement between the observed and modeled surface circulation, with monsoonal variability well captured in the model. During the SEM, the major currents identified in Figure 1 (i.e., NEMC, EACC/ZC, and SC) can be seen in both AVISO and in NEMO. The model is correctly simulating the position of the currents but the surface velocities are greater than that seen in AVISO. This is likely due to altimeters capturing only the geostrophic component of the currents whereas
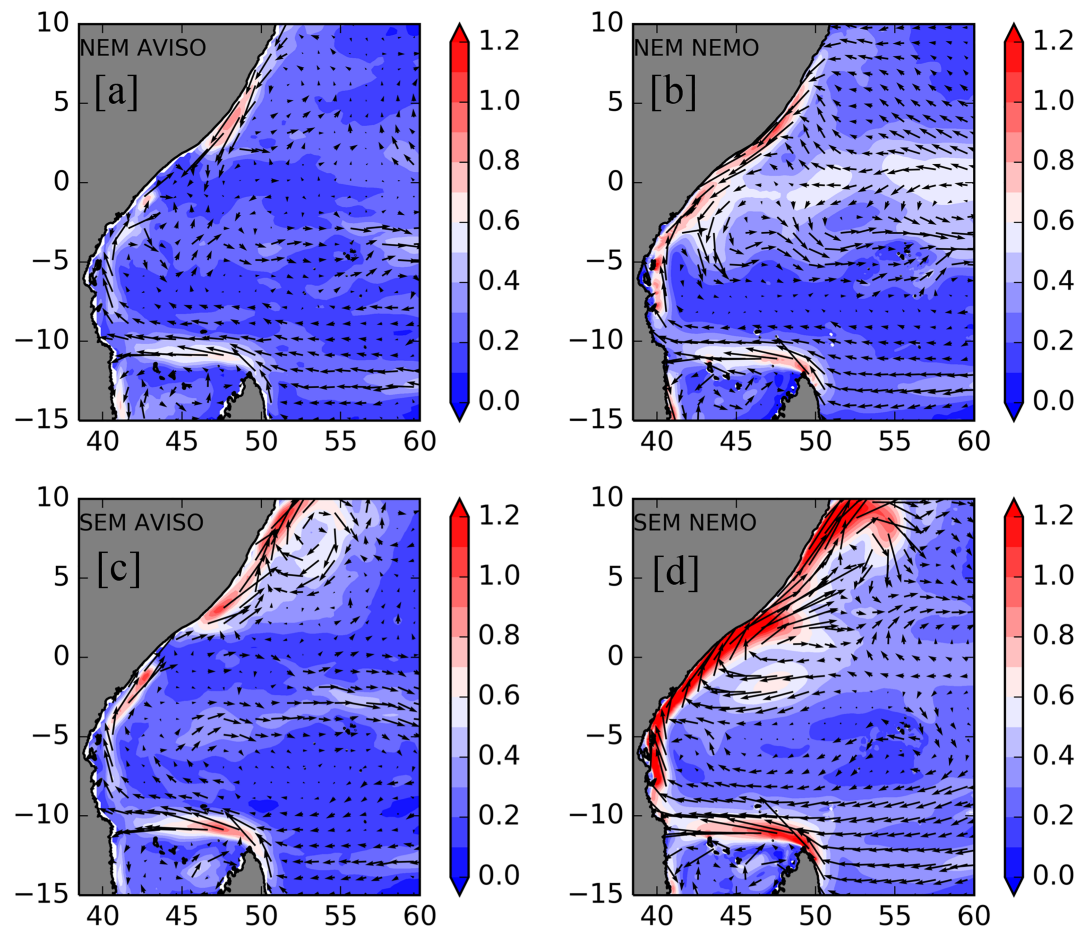
Figure 2. Decadal average of surface currents (ms^{-1}) during the NEM (DJF) and the SEM (MJJAS) (a and c) from altimetry and (b and d) from the model over the period 2001–2010. Model vectors are plotted every 3 grid points to appear consistent with AVISO.

the model captures wind-driven and other ageostrophic flows. Despite this, the model accurately represents the monsoonal variability described in section 1. Namely, the continuation of the fast (>1.2 ms^{-1}) EACC/ZC as the SC during the SEM and its eventual offshore veering to form the anticyclonic eddy known as the Great Whirl (Schott et al., 2009) north of the 5°N. It should be noted that the cross-equatorial flow of the SC is quasi-absent in the altimetry currents due to the geostrophic limitation near the equator, despite the AVISO processing including the β-plane approximation (Pujol et al., 2016).

The major monsoonal variability of the surface circulation is apparent during the NEM with reduced velocities visible in the NEMC and EACC/ZC, specifically a reduction of more than 0.5 ms^{-1} in AVISO and in NEMO. Furthermore, the reversal of the SC and resultant confluence with the EACC/ZC around 3°S is also captured by the model and, to a lesser extent, by the AVISO product. The subsequent meandering eastward flow of the SECC (0.3–0.6 ms^{-1}) is visible between the equator and 5°S, in agreement with Molinari et al. (1990). Overall, the model reproduces the key features of the WIO well, notably the position and monsoonal variability of the main currents.

As the confluence of the EACC/ZC is the subject of this paper, the focus is on the NEM period. The climatological sea surface temperature (SST) and surface chlorophyll fields during this period are shown in Figure 3 over the length of the East African coastline. To ensure consistency with the remotely sensed chlorophyll observations, which represent averages over ~17-m depths, the model outputs are averaged over the upper 15-m water depths. The model reproduces the key features of the spatial SST distribution seen in the remotely sensed field over this region with warm (>29 °C) waters observed (and modeled) south of 6°S in the open ocean and colder waters (~28 °C) along the coast of Tanzania. Distinctly colder waters (<27.5 °C) exist
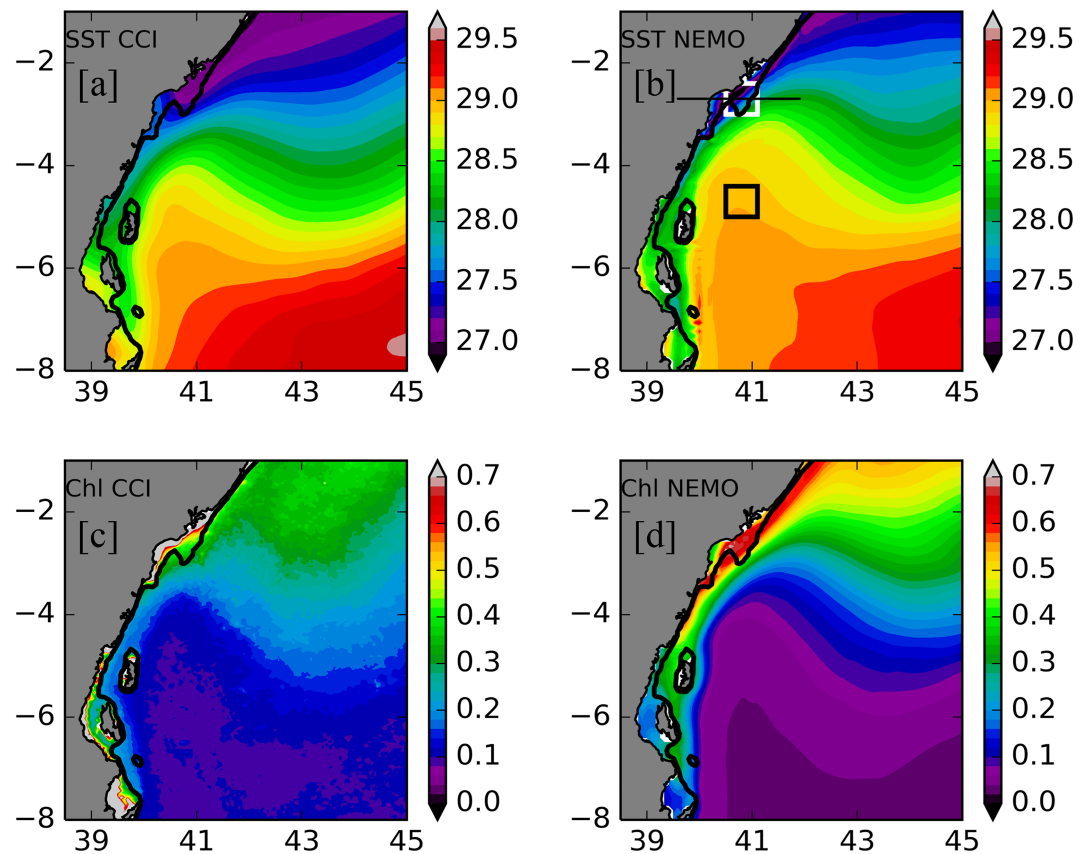
Figure 3. Decadal average of SST (°C) and surface chlorophyll (mg m^{-3}) during the NEM (DJF) (a and c) from remote sensing (CCI) and (b and d) from the model over the period 2001–2010. To follow the depth of the remotely sensed chlorophyll, the model data sets are averaged over the upper 15 m. The 200-m isobath is represented by the black line. Black and white boxes on top right panel represent regions referred to in Figures 6 and 9. Horizontal black line represents the latitude used for Figure 5.

north of 4°S and are concentrated near the Kenyan coast. This is related to wind-driven coastal upwelling from the Northeasterly winds that prevail during the NEM, which leads to offshore Ekman transport (e.g., Varela et al., 2015). Additionally, the coldest waters (<27 °C) occur near the NKBs (3°S) in the model.

The spatial pattern of surface chlorophyll is also captured by the model with relatively low chlorophyll concentrations observed (0.1 mg m^{-3}) and modeled (<0.1 mg m^{-3}) offshore and south of 4°S. The most productive waters are found further north with the highest concentrations near the coast. Interestingly, the model depicts high chlorophyll concentrations along the Tanzanian coast (~7–4.5°S) in the path of the EACC, which are not as strongly present in the observations. Overall the model well simulates the main spatial features of the region during the NEM.

3.2. Productivity Over the NKBs

Having described the large-scale variability of the key features of the ocean currents, SST, and chlorophyll, we now focus on the area surrounding the NKBs (defined here as the region where the 200-m isobath extends to 41°E; see Figure 1) during the NEM to focus on localized upwelling events. High productivity occurred over the NKBs during February 2008, used here as an example year, as demonstrated by remote sensing data shown in Figures 4a and 4b. The figure shows the large-scale latitudinal gradient observed in Figure 3, with colder, more productive waters north of the NKBs and warmer, less productive waters south of the NKBs. However, it also shows high chlorophyll concentrations of up to 1 mg m^{-3} over the NKBs (indicated by the 200-m isobath), which were associated with colder waters (25.8 °C) in comparison to the background values of ~0.5 mg/m^3 and ~26.5 °C in the surrounding waters. This is a clear cold, productive signal centered over the NKB, which is indicative of upwelling of cool, deep water.
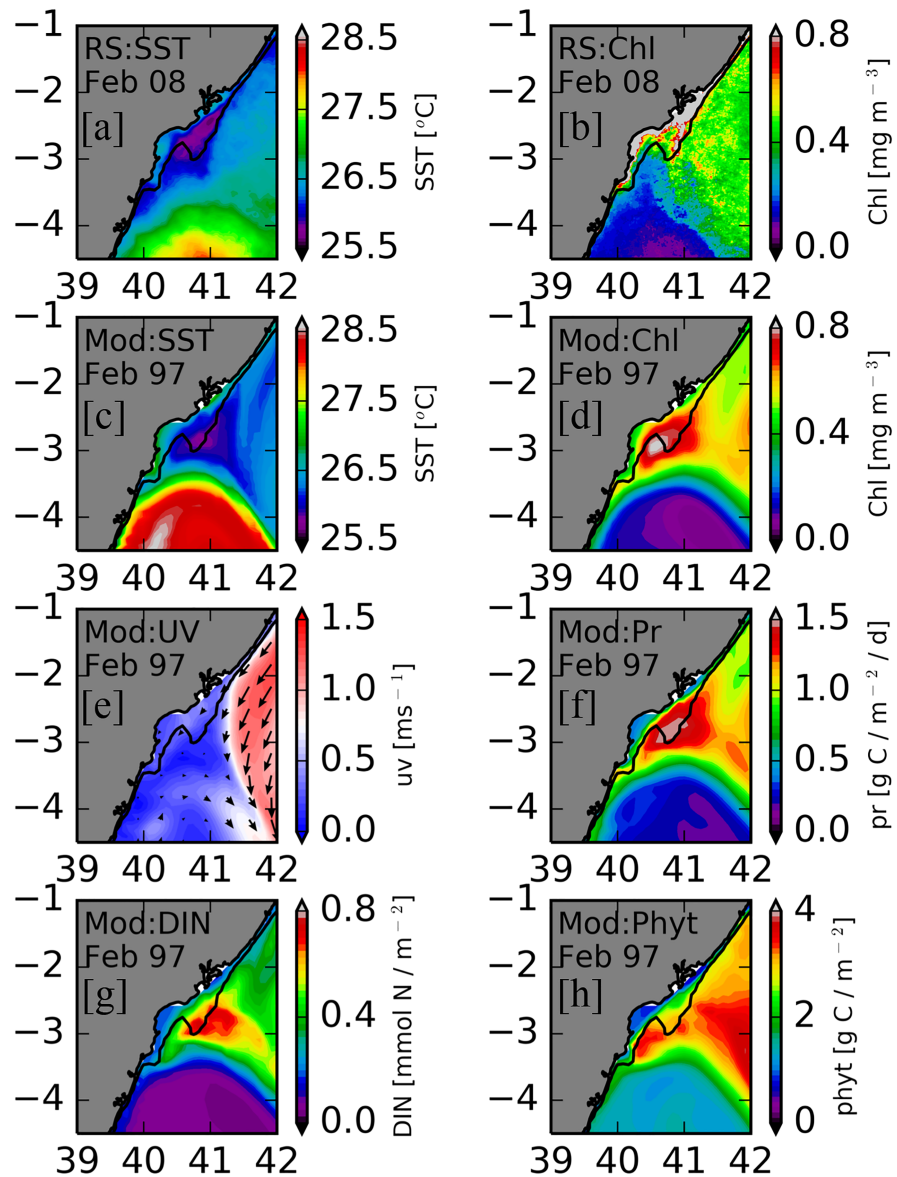
Figure 4. (a) Satellite SST (°C) and (b) surface chlorophyll (mg m^{-3}) highlight an example of high productivity on the NKB in February 2008. (c) Model SST (°C), (d) surface chlorophyll (mg m^{-3}), (e) surface currents (ms^{-1}), (f) water column-integrated primary production (g C/m^{-2}/day), (g) surface dissolved inorganic nitrogen (DIN; mmol N/m^{-2}), and (h) water column-integrated phytoplankton biomass (g C/m^{-2}) shown as a five-day mean, highlight an example of high productivity in February 1997. The black line represents the 200-m isobath. Here the surface variables are taken as the mean in the upper 15 m to ensure consistency with remote sensing.

Instances of other high productive periods are also evident in the model, with eight "strong" upwelling events identified (see section 3.3 and Figure 7). A model example, February 1997, is also shown in Figures 4c and 4d (note that this was before SeaWiFS launched so there are no corresponding remote sensing data). In 1997, the warmer, nutrient-limited waters south of the NKBs and the cooler, more productive waters north of the NKB are visible in the model with a robust upwelling signal over the NKBs. The colder (25.8 °C) SST and higher chlorophyll concentration (0.8 mg m^{-3}) are near-identical in magnitude, position, and extent to that observed in remote sensing data during February 2008. It should also be noted that there is evidence of wind-driven coastal upwelling induced by Northeasterly winds during this period (e.g., Varela et al., 2015) in both the model and in remote sensing but the upwelling signal is enhanced over the NKBs. Additionally, as can be seen in Figure 3, this enhanced upwelling signal is not clearly visible in the

climatological mean. This may be due to the considerable interannual variability so it is important to investigate the upwelling at the event scale rather than the climatological scale.

An important caveat to the analysis, is that although the model is run under a re-analysis with external forcing covering specific years, we are not able to provide a direct comparison with the satellite fields of the same year due to a considerable chaotic element in the mesoscale flow field (see a similar challenge in, e.g., Srokosz et al. (2015) and Robinson et al. (2016)). Although the model reproduces the seasonality, typical strength, shape and location of the upwelling signal, and a typical range of the interannual variability of the NKBs upwelling, we do not expect the strong upwelling years in the model to correspond exactly to the strong upwelling years observed in the remotely sensed characteristics as the mechanisms of interannual variability are complex and include both chaotic and deterministic components. Such a comparison is only possible in models which employ data assimilation.

Use of the model also enables an evaluation of water column-integrated primary production (Figure 4f) with a maximum productivity rate of up to 1.5 g C/m^{-2}/day seen over the NKBs, which is aligned with high nutrient availability, specifically dissolved inorganic nitrogen (DIN; Figure 4g). As the model does not include nutrient fluxes from sediments or rivers (but a freshwater flux), this suggests that the high productivity observed (and modeled) over the NKBs is due to upwelling as opposed to elevated outflow from the nearby Tana River. The model-integrated phytoplankton biomass also shows an elevated signal over the wider NKB region (Figure 4h). However, the peak biomass signal is located to the south between Malindi and the NKBs (see Figure 1) as opposed to directly over the NKBs like the SST, chlorophyll, productivity, and DIN signal. The origin of this feature is unclear, but could be due to advection, that is, away from the NKBs, to slow currents between Malindi and NKBs leading to an accumulation of biomass, mixing, or possibly due to a model defect. More investigation is required to understand the dynamics controlling phytoplankton biomass in this region.

The model circulation shows a fast (>1.25 ms^{-1}) SC meeting a weak EACC/ZC (<0.7 ms^{-1}) to form a confluence at ~3.5°S near the NKBs (Figure 4e) before it veers offshore as the SECC (section 1). We will henceforth refer to this at the Somali-Zanzibar Confluence Zone (SZCZ). The departure of the SC and EACC/ZC from the coast between 3.5°S and 2°S will induce upwelling at the shelf-edge, as seen in both model and remotely sensed SST and chlorophyll. It should be noted that the current speed from altimetry is more difficult to interpret near the coast than in the open ocean. This is due to the limitation of conventional satellite altimetry from which the AVISO product is derived, such as the modification of the radar echo in the vicinity of land, the inhomogeneity in the water surface observed by radar, and the less accurate corrections (Carret et al., 2019; Gommenginger et al., 2011). It is for this reason and the proximity to the equator (as discussed in section 3.1) that we do not include surface currents from altimetry here.

As the model is able to reproduce the main features of the circulation and captures upwelling events over the NKBs, the focus is to use the model to investigate the interannual variability of upwelling events and the potential mechanisms associated with them.

Using the model, cross sections across the NKBs can be examined in order to confirm if upwelling is the cause of the high productivity observed at the surface. Figure 5 shows cross sections of temperature, chlorophyll, and DIN as climatologies (Figures 5a–5c) and during February 1997 (Figures 5d–5f), a strong upwelling year (see Figure 4), across the NKBs (2.5°S; see Figure 3). In the climatology, the uplift of isotherms near the coast is visible with cooler, nutrient-rich waters being upwelled to the near-surface. For example, the 24.5°C isotherm resides at 100 m at 42°E and at 60 m at the coast, shown by the black line. Consequently, this has led to higher chlorophyll concentrations, exceeding 0.6 mg m^{-3}, in the upper 40 m but with a subsurface maximum at 20 m. The uplift of this isotherm is not visible at other times of year, that is, in the middle of the SEM in July (see Figure S1 in the supporting information) where there are deeper mixed layers and minimal isopycnal uplift toward the coast. For the February 1997 event the isotherm uplift was intensified with surface outcropping of isotherms leading to the cool anomaly (25.8°C) visible at the surface (Figure 4). The 24.5°C isotherm was raised by 70 m (120 m at 42°E and 50 m at the coast), and aligned with steeper isolines of DIN. This resulted in elevated nutrients at the surface, that is, from <0.25 mmol m^{-3} in the climatology to >0.5 mmol m^{-3} in 1997, and a higher chlorophyll concentration, exceeding 0.7 mg m^{-3}, reaching the surface as was seen in Figure 4. Thus, the upwelling is more evident at the event scale, as opposed to the climatological mean, which could indicate considerable interannual variability.
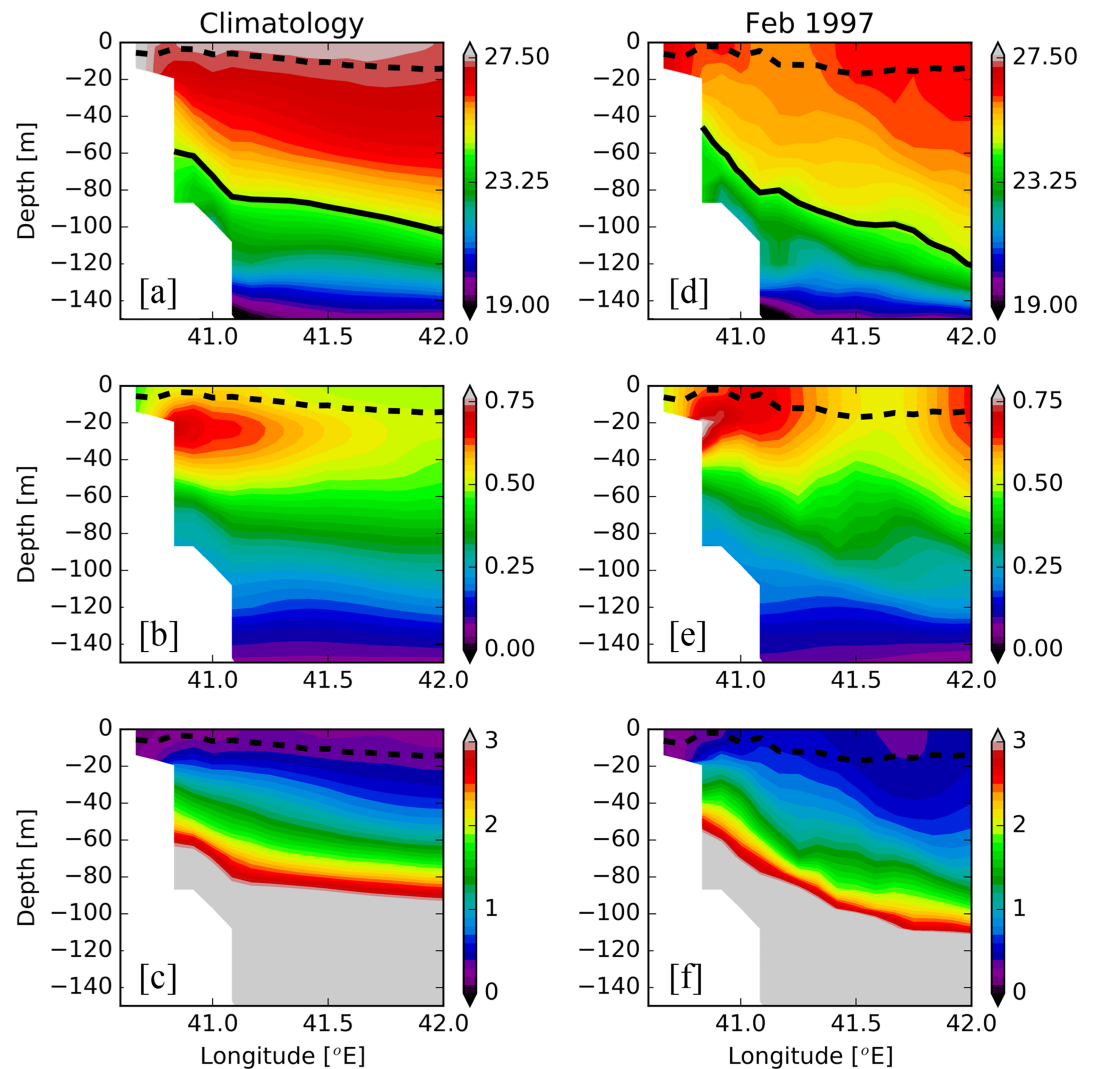
Figure 5. (left) Model-derived February decadal mean (2001–2010) and a (right) five-day mean in February 1997 of (a and d) temperature (°C), (b and e) chlorophyll (mg m^{-3}), and (c and f) dissolved inorganic nitrogen (mmol m^{-3}) shown as a cross section through the NKBs at 2.7°S (see Figure 3). The dashed black lines represent the model mixed layer depth and the black line for the top panels represent the 24.5 °C isotherm.

To further investigate the robustness of this feature, the modeled SST and water column-integrated primary production difference between two areas was taken, with the first residing inside the upwelling zone (centered on 2.7°S, 40.8°E) and the other situated outside its zone of influence (centered on 4.7°S, 40.8°E; see boxes in Figure 3). The climatological SST difference between the two areas is shown in Figure 6a with the minimum and maximum differences indicated by the dashed lines. It reveals that the greatest climatological SST difference exists during the NEM with the mean peaking in February (1.4 °C higher). This is aligned with the primary production difference (Figure 6b), which also reaches a maximum during the NEM (0.5–0.6 g C/m^{-2}/day in January and February). The lowest SST and primary production differences occur during the SEM with values close to 0 °C and 0.1 g C/m^{-2}/day, respectively, showing that there is no signature of upwelling during this season. This seasonality provides evidence that the cold, productive events over the NKB are caused by localized upwelling during the NEM as opposed to a widespread reaction to the seasonal cycle of the WIO. However, the minimum and maximum lines reveal that interannual variability exists in the strength of this upwelling with peaks of 2.2 °C and 1.1 g C/m^{-2}/day and minimum values of 0.4 °C and 0.2 g C/m^{-2}/day, respectively.
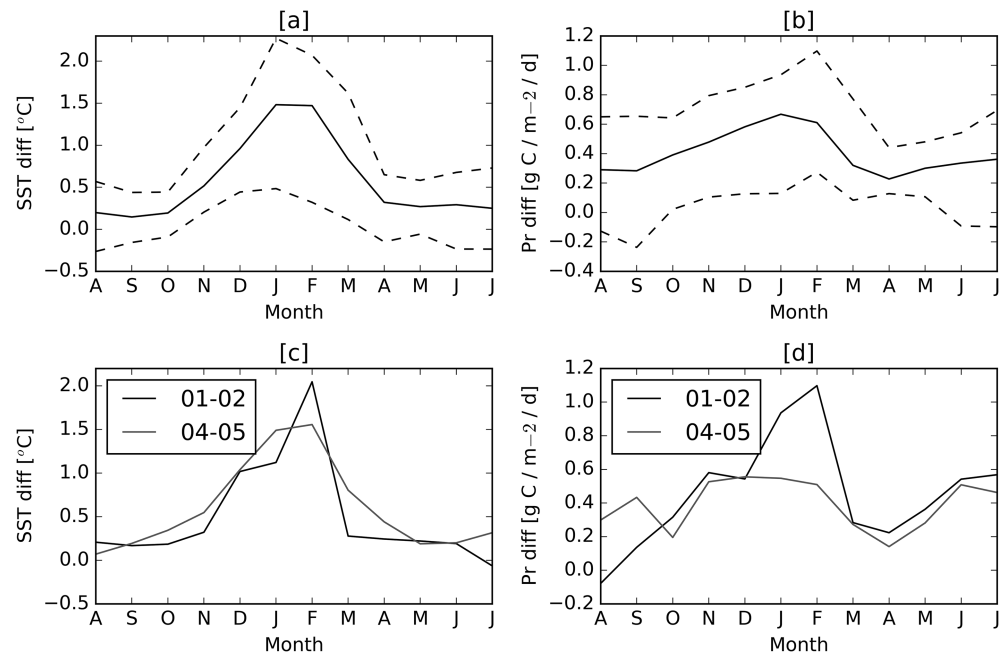
Figure 6. Modeled SST (°C; taken as the mean upper 15) and integrated primary production (g C/m^{-2}/day) difference between two stations (taken as a mean from 3–2.4°S, 40.5–41.1°E and 5–4.4°S, 40.5–41.1°E; see Figure 3) shown as (a and b) a decadal average from 2001 to 2010 with the dashed lines representing the range for each month during the same period (top). (c and d) The progression of the SST and primary production difference between these two stations is also shown for a strong event (2001–2002; black line) and a relatively weak event (2004–2005; green line) from August to July (bottom).

The progression of the SST and water column-integrated primary production difference for a strong upwelling event (2002) and a relatively weak upwelling event (2006) is shown in Figures 6c and 6d. These years represent examples of a strong and weak upwelling year, respectively. For both events, the greatest temperature differences in the climatology occur during the NEM months, which suggests that the climatology is not dominated by a few strong events and some degree of upwelling occurs over the NKBs in most years. For example, even during the weak event of 2006 the SST (primary production) difference between the two stations reaches 1.5 °C (0.5 g C/m^{-2}/day) during February but with an overall elevated productivity from November to February, which is coherent with Figure 3 and is related to coastal upwelling induced by Northeasterly winds during this period (e.g., Varela et al., 2015). A similar productive period exists during the strong 2002 event but a clear peak occurs from January to February. The SST difference reaches 2 °C in February with a corresponding surface primary production difference exceeding 1.1 g C/m^{-2}/day, equivalent to a 33% and 120% increase compared to the weak event.

It is clear from Figures 4–6 that shelf-edge upwelling is responsible for the cold, productive signal that can appear over the NKBs during the NEM, which is likely enhanced by wind-driven coastal and topographic upwelling. Furthermore, considerable interannual variability exists in the intensity of this upwelling feature, which is explored in section 3.3.

3.3. Interannual Variability in NKB Upwelling

Figure 7a shows the mean water column-integrated primary production from 1993 to 2015 during the NEM (averaged for January and February when the upwelling signal is greatest). It shows a "background" productivity level of about 1.0 g C/m^{-2} along the coast with elevated levels on the inner NKBs (from 40.5 to 41°E; see black box) and by the smaller topographic feature further south at around 3.5°S near Malindi (see Figure 1). From this we see that this region experiences some degree of wind-driven coastal upwelling every year associated with offshore Ekman transport from the prevailing Northeasterly winds (e.g., Varela et al., 2015). This is also apparent in Figure S2, which shows the same maps for SST and DIN, with cooler SSTs of 27.25 °C and an elevated DIN signal of 0.3 mmol N m^{-2} seen along the coast. Figure 7a also indicates
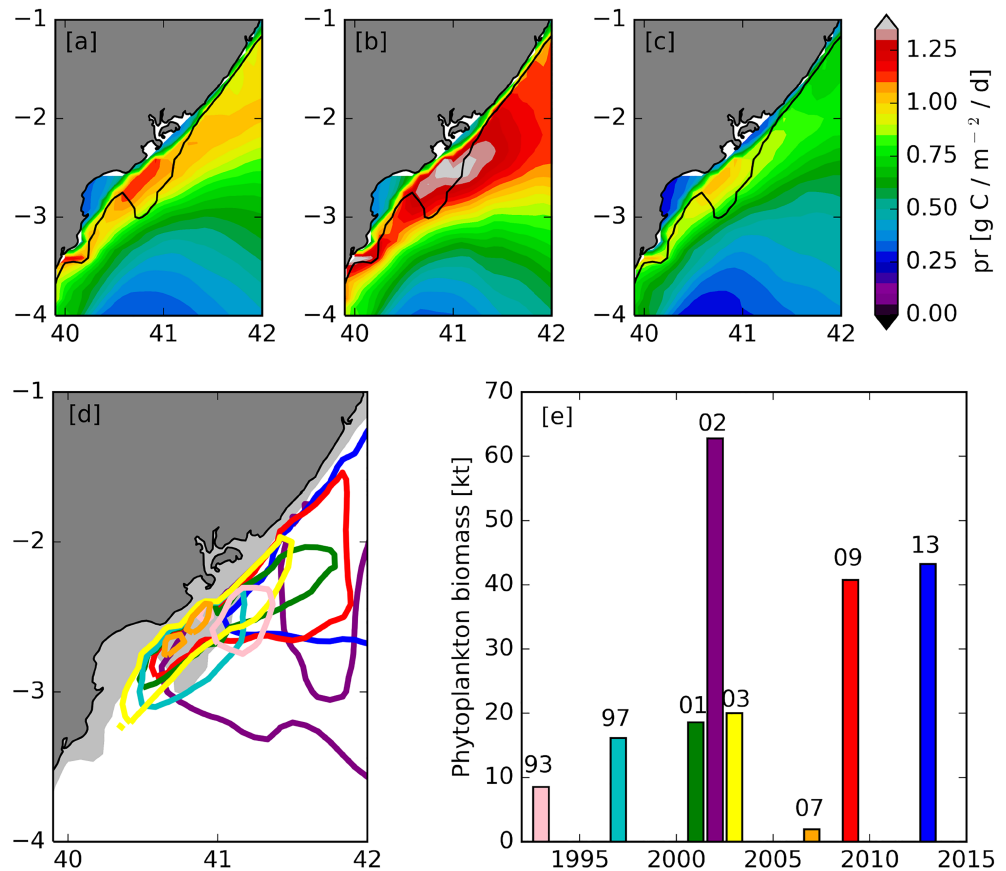
Figure 7. Model water column-integrated primary production (g C/m^{-2}/day) over the NKB region shown as (a) an average for January and February 1993–2015, during (b) strong upwelling years (specified in text) and (c) weak upwelling years. (d) Primary production contours of 1.3 g C/m^{-2}/day for January and February 1993–2015, only years with primary production exceeding 1.3 g C/m^{-2}/day are shown with the colors corresponding to the years shown in (e) (light grey shading denotes the continental shelf inside 200 m). Contours associated with solely wind-driven coastal upwelling have been filtered out. (e) Three-dimensionally integrated phytoplankton biomass (kilo-tonnes C) from the region inside the contours defined in (d). Black box in (a) highlights region characterized by high background productivity.

that the upwelling is topographically enhanced over the NKBs and over the topographic feature near Malindi with rates exceeding 1.15 g C/m^{-2}/day.

Figures 7b and 7c show primary production rates for strong and weak upwelling years, respectively (the corresponding SST and DIN is shown in Figure S2). Strong upwelling years are characterized as years where water column-integrated primary production exceeds 1.3 g C/m^{-2}/day over the NKB region in either January or February (1993, 1997, 2001, 2002, 2003, 2007, 2009, and 2013). "Weak" upwelling years are years where primary production falls below this value or is located along the coast only. This threshold value is largely arbitrary but based on high productivity rates over the NKBs that are not associated with the wind-driven coastal upwelling that occurs every year.

During strong upwelling years, primary production is enhanced along the coastline (~1.2 g C/m^{-2}/day) but higher productivity also extends further east of the NKBs. Values exceeding 1.3 g C/m^{-2}/day are found over the NKBs from 2.8 to 2.2°S. In contrast, during weak upwelling years, reduced rates of primary production occur along the coast (~0.75 g C/m^{-2}/day) with productivity rates less than 1 g C/m^{-2}/day over the NKBs. There is always some level of productivity along the coast during the NEM, associated with Ekman-induced upwelling, with further elevated productivity over the inner NKBs, which is topographically enhanced. Additionally, there are strong upwelling events that occur in some years, which further intensifies the productivity over the outer NKBs and often covering a much larger area.

The spatial extent of the upwelling signal for each strong year is shown in Figure 7d, where the 1.3 g C/m^{-2}/day water column-integrated primary production contour is used to define the geographical extent. Due to the substantial spatial variability in primary production over the area of interest, it is difficult to find an objective method of selecting a single threshold value delineating the upwelling area which would be applicable to all years. Thus, the value of 1.3 g C/m^{-2}/day is chosen subjectively by visual analysis of the interannual variability and climatological mean (the latter is visible in Figure 7b).

Additionally, Figure 7e quantifies the amount of upwelling-induced biomass by calculating the water column-integrated phytoplankton biomass within these contours, that is, integrating over the surface area of each contour seen in Figure 7d. It is evident that considerable variability exists across these years in terms of total phytoplankton biomass, in the region of high primary production, and the spatial extent of the upwelling. For example, 2002 (shown in Figures 7d and 7e in purple) stands out as a year with very high productivity with a total phytoplankton biomass of over 60 kt C. High productivity exists over a large area extending into the open ocean and 2002 was also an anomalous year across the WIO region (Kumar et al., 2006; Krishnan et al., 2006), which could suggest that multiple mechanisms are at play. It should be noted that the larger area of productivity occurring in 2002 will, of course, lead to a greater phytoplankton biomass than years with high productivity affecting a smaller area, that is, in 1993 and 2007.

In 2009 and 2013 there was more than 40 kt of phytoplankton biomass, which resides over a large region north of (and including) the NKBs. Like 2002, these years exhibit high productivity over a large region, contributing to the high phytoplankton biomass calculated in Figure 7e. Even though both of these signals cover part of the NKBs, the high productivity includes the region further north of the NKBs. All remaining strong upwelling years have a phytoplankton biomass ranging from 3 to 20 kt C, which resides on and around the NKBs. Although the spatial extent and position of upwelling varies from year-to-year, part of the upwelling is always rooted to the NKBs, which supports the idea that this mechanism may indeed impact recruitment in the NKB fishery. However, the question still remains: what is initiating these upwelling events?

As indicated in section 1, the NEM leads to the reversal of the alongshore wind field and induces the southward flow of the SC which meets the northward flowing EACC/ZC to form the SZCZ. For the 1997 upwelling event (Figure 4), the SZCZ was situated near the NKBs. We have shown that the confluence region is associated with slope upwelling which promotes greater primary production. This raises the question of whether the north-south movement of the confluence zone between years could explain the interannual variability of upwelling and productivity over the NKBs. To answer this question the model is used to locate the position of the SZCZ, track its progression along the coast during the NEM, and relate this to upwelling intensity over the NKBs.

We define the SZCZ as the latitude where the northward flowing EACC/ZC meets the southward flowing SC. To calculate this, we take the maximum latitude of the 0-ms^{-1} meridional velocity contour, that is, the point where the meridional velocity goes from positive (EACC/ZC) to negative (SC), over the region 6°S–1°N, 39°E–44°E. The latitude of the SZCZ from December to February over the period 1993–2015 is shown in Figure 8; note that any gaps for December correspond to periods when the SZCZ had yet to form. The time series shows a general southward movement of the SZCZ from December to February. In December, if clearly formed, the SZCZ can be located as far north as 1°N or as far south as 2°S with an average latitude of 0.27°S. In January, its mean position is 2.27°S, but ranges from 4 to 1.2°S for individual years, and by February it reaches its southernmost position with a mean position of 2.87°S. In February, however, the interannual range in the position of the SZCZ extends to more than 4° of latitude with the SZCZ being located between 6 and 1.9°S in any given year.

The SZCZ resides in a very complex region where both atmospheric and oceanic processes affect many aspects of WIO variability. Consequently, there are likely multiple mechanisms responsible for the timing of the SZCZ formation and for the variability of its position. For example, the onset of the NEM wind field is responsible for the reversal of the upper SC (Schott et al., 2002), but interannual variability in the strength of the wind field will likely affect the position of the SZCZ. Furthermore, the intensity of the SC and EACC/ZC are also influenced by changes in the wider Indian Ocean and in the case of the EACC/ZC, interannual variability in the strength/transport of the SEC may also be important. The Indian Ocean also experiences periodic oscillations in SST driven by the IOD and is also strongly affected by ENSO driven changes in
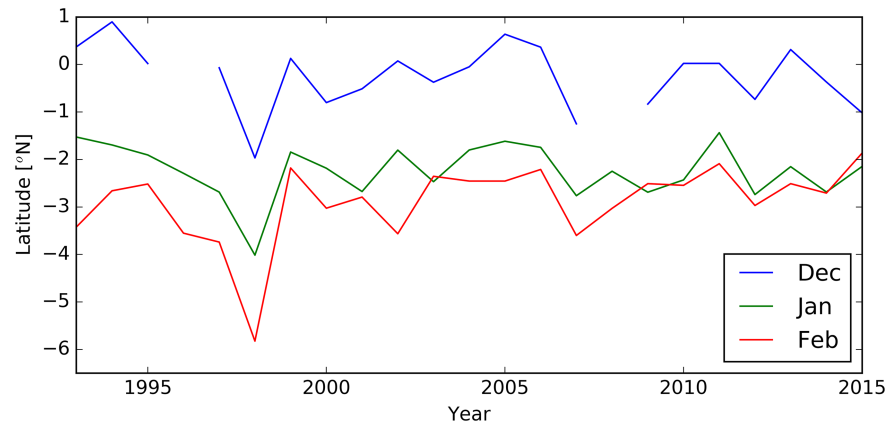
Figure 8. Latitude (deg) of the SZCZ in December, January, and February from 1993 to 2015. The SZCZ is defined as the maximum latitude of the 0-ms^{-1} meridional velocity contour in the region 6°S–1°N, 39°E–44°E.

SST (e.g.,Saji et al., 1999 ; Webster et al., 1999 ; Wiggert et al., 2009), both of which may have an impact on the position of the SZCZ.

There is one anomalous event visible in the confluence zone time series that both supports the influence of teleconnections on the position of the confluence zone and which also skews the 1993–2015 mean position of the confluence zone. This event, in 1998, saw the SZCZ reach as far as 6° in February, which is adjacent to the coast of Zanzibar Island (Tanzania), during the major El Niño event of 1997–1998. Subsequent El Niño events were less significant in their impact (if at all) and investigation of the causes, and consequences, of the extreme southerly positioning of the SZCZ during 1998 should be the focus of future research efforts.

Discounting the anomalous year of 1998, the SZCZ typically resides between 2 and 4°S, which is in agreement with previous studies (Mayorga-Adame et al., 2016; Schott et al., 2009). Here we investigate to what extent the variability in the SZCZ position influences the intensity of upwelling and consequent productivity of the NKBs. As February is the month that experiences the greatest SST and primary production difference (Figure 6) and the southernmost SZCZ (Figure 8) we will focus on the variability during this month only.

Figure 9 shows the position of the SZCZ in February (as in Figure 8) alongside the mean February SST, water column-integrated primary production, surface DIN, and the total integrated phytoplankton biomass over the NKB box from 3–2.4°S, 40.5–41.1°E (see Figure 3). These four variables are taken to represent the intensity of upwelling over the NKBs and are assessed alongside the position of the SCZC to determine if a relationship exists. The mean SST over the NKBs during February is 27.7 °C, ranging from 26.26 to 29.46 °C with the cooler temperatures associated with a SZCZ that is positioned relatively further to the south. The mean primary production is 0.9 g C/m^{-2}/day, ranging from 0.44 to 1.36 g C/m^{-2}/day with elevated productivity rates occurring when the SZCZ is further south and SST is cooler. These years are also associated with the highest concentrations of DIN, which range from 0.06 to 0.62 mmol N m^{-2} with an average of 0.28 mmol N m^{-3}. Additionally, the total phytoplankton biomass, integrated three-dimensionally over the NKB box, ranges from 16 kt in 1998 to 31 kt in 2002 with a mean 22 kt over the NKBs.
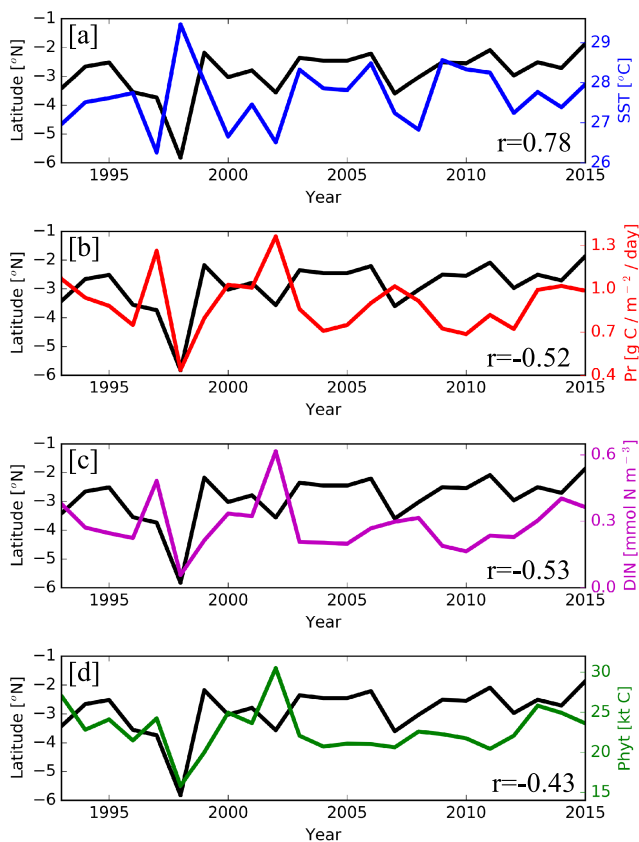
Figure 9. Latitude (deg) of the SZCZ (black line; transferred from Figure 8) with mean (a) SST (°C; blue line), (b) water column-integrated primary production (g C/m^{-2}/day; red line), (c) dissolved inorganic nitrogen (mmol m^{-3}; purple line), and (d) the total integrated phytoplankton (kt C; green line) over the NKBs (3–2.4°S, 40.5–41.1°E; see Figure 3) in February from 1993 to 2015.

Excluding 1998, the monthly mean SST is correlated ($r = 0.78$, $p < 0.05$) with the latitude of the SZCZ, while an anticorrelation exists with primary production ($r = -0.52$, $p < 0.05$), surface DIN ($r = -0.53$, $p < 0.05$), and total integrated phytoplankton ($r = -0.43$, $p < 0.05$). This suggests that when the SZCZ is located further south, that is, in the range 4–3°S, colder, more productive, nutrient-rich waters exist over the NKBs, indicating enhanced upwelling, which leads to a greater phytoplankton biomass. Greater upwelling intensity over the NKBs, induced by a more southerly position of the SZCZ, could therefore be a significant factor supporting the NKB fishery.

As we saw in Figure 7, the upwelling often affects a wider area (Figures 7b and S2). The greatest integrated phytoplankton biomass occurred during 2002 (Figure 7e) where the upwelling affected the largest area (Figure 7d). However, the peak biomass signal is not just due to covering a greater area as it stands out as a clear maximum when averaging over the NKB (Figure 9d). Furthermore, except 2007, all strong upwelling years seen in Figure 7 have above average phytoplankton biomass over the NKB box (Figure 9). Figure 7d shows that the region of high productivity (i.e., >1.3 g C/m^{-2}/day) in 2007 covers a small area, specifically smaller than the NKB box, which is likely why it is not noticeable as an anomalous year over the NKBs in Figure 9. Additionally, Figure 9 calculates phytoplankton biomass in February, when the SZCZ resides relatively further south, whereas Figure 7 investigates strong upwelling events over January and February, which may also lead to slightly different results.

4. Discussion and Conclusions

Using a high-resolution, global, biogeochemical ocean model, we have calculated the variability in the position of the SZCZ that forms during the NEM. The model performs well in the WIO region accurately capturing the position and monsoonal variability of the surface circulation. Specifically, the reversal of the SC during the NEM and formation of the SZCZ between 4 and 2°S, is in agreement with prior studies (Mayorga-Adame et al., 2016; Schott et al., 2009). The model also simulates the appearance of cooler more productive waters over the NKB during the NEM and is able to reproduce strong upwelling events observed in remote sensing data sets including the location, seasonality, and typical strengths.

This study has demonstrated that some degree of wind-driven coastal upwelling occurs along the wider Kenyan coastline every year during the months of the NEM with additional topographic enhancement over the NKBs. This upwelling of colder, nutrient-rich water led to greater productivity over the NKBs with depth-integrated primary production enhanced by up to 1.1 g C/m^{-2}/day compared to far-field waters. Upwelling occurs only during the months of the NEM and peaks between December and February, yet its impact is not evident in the annual mean fields of SST and primary production even during years when the strongest upwelling occurs, suggesting that its significance has been overlooked.

We find that there is interannual variability in the impact of upwelling during the months of January or February over the period 1993–2015. Due to this variability, it is important to investigate the upwelling at the event scale rather than the climatological scale. Factors likely to be driving this variability include variations in the wind field, in the eastward flow of the SECC which induces divergence from the coast, in the strength of global teleconnections (e.g., ENSO and IOD), and more locally in current-topographic interactions. Here we focused on the position of the SZCZ, which is the origin of the eastward flow of the SECC and forms during the NEM (Figure 8).

Over the NKBs, the strongest upwelling events, characterized by high rates of primary production (Figure 9), occurred in 1993, 1997, 2002, and 2007 when the SZCZ was found south of 3°S, and thus south of the NKBs. SST over the NKBs is significantly correlated with the latitude of the SZCZ with significant anticorrelations found for primary production, DIN, and integrated phytoplankton biomass. This provides evidence that the SZCZ exerts a control on the amount of upwelling, and therefore productivity, over the NKBs. Even though shelf-edge upwelling during strong upwelling years is always connected to the NKBs, there is considerable interannual variability in the intensity and spatial extent of any resulting productivity or SST signal. For example, in 2009 and 2013, when enhanced upwelling led to over 40-kt C integrated phytoplankton biomass, the main upwelling signal was found mostly to the north of the NKBs, that is, north of 2.5°S (Figure 7), with the SZCZ also positioned further north (Figure 8). There are also other instances where the SZCZ resides near 2.5°S, but where productivity rates do not exceed 1.3 g C/m^{-2}/day (Figure 7). However, for the four years where the SZCZ was positioned directly over the NKBs, an upwelling signal was always present.

Here we have established that the position of the SZCZ exerts a strong control on the amount of upwelling over the NKBs, which raises the question, what causes the north-south movement of the SZCZ? The position of the SZCZ is likely controlled by the strength of the EACC/ZC and SC, which are strongly dependent on the strength of the wind stress (e.g., Schott et al., 2002). Additionally, modeled currents in February 1997 (Figure 4) show a weak northward flowing EACC pushing a strong southward flowing SC offshore, which could suggest that vorticity conservation is important, as first proposed by Johnson et al. (1982). Furthermore, the ENSO, IOD, and MJO are known to induce changes in the WIO (e.g., Saji et al., 1999; Webster et al., 1999; Zhang et al., 2005) and may be interacting with the wind field to induce changes in the formation and variability of the SZCZ. More investigation is required to identify the relative importance of these mechanisms and how they collectively influence the position of the SZCZ, especially given the role upwelling over the NKBs may have for supporting fisheries in the region.

In addition to the ENSO and IOD potentially exerting interannual variability on the position of the SZCZ, they may also have an impact on the strength of the upwelling signal over the NKBs. For example, the strong upwelling event that occurred in 1997 coincided with a major negative IOD event (with a lag of one to two months), which indicates that the WIO was cooler and had a shallower thermocline than the eastern Indian Ocean (e.g., Saji et al., 1999). Additionally, there is in situ and modeled evidence that cool SSTs and elevated DIN (both evidence of increased upwelling) existed over the NKBs during 1997 (Obura, 2001; Webster et al., 1999). Conversely, the following year (1998) saw a major El Niño that coincided with a positive IOD event, which led to widespread anomalous warming in the WIO (e.g.,Saji et al., 1999 ; Webster et al., 1999). This impact was reproduced by the model and during this time the SZCZ was located more than 3° further south relative to its mean position (Figure 9). This may have had a detrimental effect on the upwelling over the NKBs and will be the subject of a future paper.

Here we have shown that the ocean circulation exerts an important control on the productivity over the NKBs, which is now emerging as a new frontier for food security (e.g., Akunga, 2007). Thus, improving our understanding of the upwelling mechanism responsible for elevated productivity, and for any interannual variability in that productivity, is important. It is, however, vital that new in situ observations are made to better understand the consequences of shelf-edge upwelling for the NKB ecosystem and to better validate biogeochemical models used for understanding the dynamics of the area and the consequences for fisheries.

References

Akunga, B. G. (2007). *Influence of climate variability on coastal small-scale Fishing communities in kenya. PhD N85/10656/2007 the School of Environmental studies of Kenyatta University*.

Al-Naimi, N., Raitsos, D., Ben-Hamadou, R., & Soliman, Y. (2017). Evaluation of satellite retrievals of chlorophyll-*a* in the Arabian Gulf. *Remote Sensing*, *9*(3), 301. https://doi.org/10.3390/rs9030301

Barnes-Mauthe, M., Oleson, K. L., & Zafindrasilivonona, B. (2013). The total economic value of small-scale fisheries with a characterization of post-landing trends: An application in Madagascar with global relevance. *Fisheries Research*, *147*, 175–185. https://doi.org/10.1016/j.fishres.2013.05.011

Bendeković, J., & Vuletić, D. (2013). Piracy influence on the shipowners and insurance companies. In *DAAAM International Scientific Book 2013* (Chap. 42, pp. 711–718). DAAAM International Viennna: DAAAM International Publishing. https://doi.org/10.2507/daaam.scibook.2013.42

Brodeau, L., Barnier, B., Penduff, T., Treguier, A.-M., & Gulev, S. (2010). An ERA 40 based atmospheric forcing for global ocean circulation models. *Ocean Modelling*, *31*, 88–104. https://doi.org/10.1016/j.ocemod.2009.10.005

Bruce, J. G. (1970). Notes on the Somali current system during the Southwest Monsoon. *Journal of Geophysical Research*, *75*(21), 4170–4173. https://doi.org/10.1029/JC075i021p04170

Bultel, E., Doherty, B., Herman, A., Le Manach, F., & Zeller, D. (2015). An update of the reconstructed marine fisheries catches of Tanzania with taxonomic breakdown. In F. Le Manach & D. Pauly (Eds.), *Fisheries catch reconstructions in the Western Indian Ocean, 1950–2010*, *Fisheries Centre Research Reports* (Vol. 23, pp. 151–161). Vancouver: Fisheries Centre, University of British Columbia. [ISSN 1198–6727]

Carret, A., Birol, F., Estournel, C., Zakardjian, B., & Testor, P. (2019). Synergy between in situ and altimetry data to observe and study Northern Current variations (NW Mediterranean Sea). *Ocean Science*, *15*(2), 269–290. https://doi.org/10.5194/os-15-269-2019

Cherkasheva, A., Nothig, E. M., Bauerfeind, E., Melsheimer, C., & Bracher, A. (2013). From the chlorophyll-*a* in the surface layer to its vertical profile: A Greenland Sea relationship for satellite application3; Arrigo et als. *Ocean Science*, *9*(2), 431–445.

Dai, A., & Trenberth, K. E. (2002). Estimates of freshwater discharge from continents: Latitudinal and seasonal variations. *Journal of Hydrometeorology*, *3*(6), 660–687. https://doi.org/10.1175/1525-7541(2002)003<0660:EOFDFC>2.0.CO;2

Düing, W., & Schott, F. (1978). Measurements in the source region of the Somali Current during the monsoon reversal. *Journal of Physical Oceanography*, *8*(2), 278–289. https://doi.org/10.1175/1520-0485(1978)008<0278:MITSRO>2.0.CO;2

Dussin, R., Barnier, B., Brodeau, L., & Molines, J.-M. (2016). The making of Drakkar forcing set DFS5, DRAKKAR/MyOcean Report, 01-04-16, LGGE, Grenoble, France. https://www.drakkarocean.eu/publications/reports/report_DFS5v3_April2016.pdf

Embling, C. B., Sharples, J., Armstrong, E., Palmer, M. R., & Scott, B. E. (2013). Fish behaviour in response to tidal variability and internal waves over a shelf sea bank. *Progress in Oceanography*, *117*, 106–117. https://doi.org/10.1016/j.pocean.2013.06.013

FAO. (2016). [KENYA] National Report to the Scientific Committee of the Indian Ocean Tuna Commission, 2016 IOTC–2016–SC19–NR13

Fieux, M. (2001). Somali current. In J. H. Steele, et al. (Eds.), *Encyclopedia of Ocean Sciences* (pp. 2839–2849). San Diego, CA: Academic.

Fulanda, B., Ohtomi, J., Mueni, E., & Kimani, E. (2011). Fishery trends, resource-use and management system in the Ungwana Bay fishery Kenya. *Ocean and Coastal Management*, *54*(5), 401–414. https://doi.org/10.1016/j.ocecoaman.2010.12.010

Gommenginger, C., Thibaut, P., Fenoglio-Marc, L., Quartly, G., Deng, X., Gómez-Enri, J., et al. (2011). Retracking altimeter waveforms near the coasts. In *Coastal altimetry* (pp. 61–101). Berlin, Heidelberg: Springer. https://doi.org/10.1007/978-3-642-12796-0_4

Gordon, H. R., & Morel, A. Y. (1983). *Remote assessment of ocean color for interpretation of satellite visible imagery: A review* (p. 114). Berlin: Springer-Verlag.

Hellerman, S., & Rosenstein, M. (1983). Normal monthly wind stress over the world ocean with error estimates. *Journal of Physical Oceanography*, *13*(7), 1093–1104. https://doi.org/10.1175/1520-0485(1983)013<1093:NMWSOT>2.0.CO;2

IOCCG (2000). Remote sensing of ocean colour in coastal and other optically complex waters. In S. Sathyendrannath (Ed.), *Reports of the International Ocean Colour Coordinating Group* (Vol. 3, Chap. 2, pp. 23–46). Dartmouth, Canada: IOCCG.

Jackson, T., Sathyendranath, S., & Mélin, F. (2017). An improved optical classification scheme for the Ocean Colour Essential Climate Variable and its applications. *Remote Sensing of Environment*, *203*, 152–161. https://doi.org/10.1016/j.rse.2017.03.036

Johnson, D. R., Nguli, M. M., & Kimani, E. J. (1982). Response to annually reversing monsoon winds at the southern boundary of the Somali Current. *Deep Sea Research*, *29*, 1217–1227. https://doi.org/10.1016/0198-0149(82)90091-7

Jury, M., McClanahan, T., & Maina, J. (2010). West Indian Ocean variability and East African fish catch. *Marine Environmental Research*, *70*(2), 162–170. https://doi.org/10.1016/j.marenvres.2010.04.006

Kabanova, Y. G. (1968). Primary production of the northern Indian Ocean. *Oceanologica*, *8*, 214–223.

Kitheka, J. U. (2002). Freshwater and sediment discharge in Ungwana bay: The role of the Tana and Sabaki rivers. http://www.oceandocs.org/bitstream/1834/927/1/Ungwana2002.pdf

Krishnan, R., Ramesh, K. V., Samala, B. K., Meyers, G., Slingo, J. M., & Fennessy, M. J. (2006). Indian Ocean-monsoon coupled interactions and impending monsoon droughts. *Geophysical Research Letters*, *33*, L08711. https://doi.org/10.1029/2006GL025811

Kumar, K. K., Rajagopalan, B., Hoerling, M., Bates, G., & Cane, M. (2006). Unraveling the mystery of Indian monsoon failure during El Niño. *Science*, *314*(5796), 115–119. https://doi.org/10.1126/science.1131152

Le Manach, F., Abunge, C. A., McClanahan, T. R., & Pauly, D. (2015). Tentative reconstruction of Kenya's marine fisheries catch, 1950–2010. In F. Le Manach & D. Pauly (Eds.), *Fisheries catch reconstructions in the Western Indian Ocean, 1950–2010*, *Fisheries Centre Research Reports* (pp. 37, 23–51). Vancouver: Fisheries Centre, University of British Columbia. [ISSN 1198–6727]

Lee, Z. P., Darecki, M., Carder, K. L., Davis, C. O., Stramski, D., & Rhea, W. J. (2005). Diffuse attenuation coefficient of downwelling irradiance: An evaluation of remote sensing methods. *Journal of Geophysical Research*, *110*, C02016. https://doi.org/10.1029/2004JC002275

Leetmaa, A., Quadfasel, D. R., & Wilson, D. (1982). Development of the flow field during the onset of the Somali Current, 1979. *Journal of Physical Oceanography*, *12*(12), 1325–1342. https://doi.org/10.1175/1520-0485(1982)012<1325:DOTFFD>2.0.CO;2

Levitus, S., Conkright, M., Boyer, T. P., O'Brian, T., Antonov, J., Stephens, C., et al. (1998). World ocean database 1998. Technical report NESDIS 18, NOAA Atlas

Liao, X., Du, Y., Zhan, H., Wang, T., & Feng, M. (2017). Wintertime phytoplankton blooms in the western equatorial Indian Ocean associated with the Madden-Julian Oscillation. *Journal of Geophysical Research: Oceans*, *122*, 9855–9869. https://doi.org/10.1002/2017JC013203

Madec, G. (2015). NEMO ocean engine.

Mahongo, S. B., Francis, J., & Osima, S. E. (2011). Wind patterns of coastal Tanzania: Their variability and trends. *Western Indian Ocean Journal of Marine Science*, *10*(2), 107–120.

Maina, G. W. (2012). A baseline report for the Kenyan small and medium marine pelagic fishery. https://www.oceandocs.org/bitstream/handle/1834/6835/ktf0262.pdf?sequence=1

Marzocchi, A., Hirschi, J. J. M., Holliday, N. P., Cunningham, S. A., Blaker, A. T., & Coward, A. C. (2015). The North Atlantic subpolar circulation in an eddy-resolving global ocean model. *Journal of Marine Systems*, *142*, 126–143. https://doi.org/10.1016/j.jmarsys.2014.10.007

Mayorga-Adame, G. C., Ted Strub, P., Batchelder, H. P., & Spitz, Y. H. (2016). Characterizing the circulation off the Kenyan-Tanzanian coast using an ocean model. *Journal of Geophysical Research: Oceans*, *121*, 1377–1399. https://doi.org/10.1002/2015JC010860

McClanahan, T. R. (1988). Seasonality in East Africa's coastal waters. *Marine Ecology Progress Series*, *44*, 191–199.

McClanahan, T. R., & Obura, D. (1997). Sedimentation effects on shallow coral communities in Kenya. *Journal of Experimental Marine Biology and Ecology*, *209*, 103–122. https://doi.org/10.1016/S0022-0981(96)02663-9

McClanahan, T. R., & Young, T. P. (1996). *East African ecosystems and their conservation* (p. 100). New York: Oxford University Press.

Moat, B. I., Josey, S. A., Sinha, B., Blaker, A. T., Smeed, D. A., McCarthy, G., et al. (2016). Major variations in subtropical North Atlantic heat transport at short (5 day) timescales and their causes. *Journal of Geophysical Research: Oceans*, *121*, 3237–3249. https://doi.org/10.1002/2016JC011660

Molinari, R. L., Olson, D., & Reverdin, G. (1990). Surface current distributions in the tropical Indian Ocean derived from compilations of surface buoy trajectories. *Journal of Geophysical Research*, *95*(C5), 7217–7238. https://doi.org/10.1029/JC095iC05p07217

Morgans, J. F. C. (1959). The north Kenya banks. *Nature*, *184*(4682), 259. https://doi.org/10.1038/184259b0

Mwangi, S. N. (2002). Water quality and productivity of the Malindi-Ungwana Bay fishing grounds. *Current status of trawl fishery of Malindi-Ungwana Bay—Final report. Kenya Marine and Fisheries Research Institute (KMFRI), Mombasa (Kenya)*, 30-42.

Ngusaru, A. S., & Mohammed, M. S. (2002). Water, salt and stoichiometrically linked nutrient budget for Chwaka Bay, Tanzania.

Nyandwi, N. (2013). The effects of monsoons on the East African coastal current through the Zanzibar Channel, Tanzania. *Journal of Ocean Technology*, *8*(4).

Obura, D. O. (2001). Kenya. *Marine Pollution Bulletin*, *42*(12), 1264–1278.

Ochumba, P. B. (1983). Oceanographic features along the Kenyan Coast: Implications for fisheries management and development.

Palmer, M. R., Inall, M. E., & Sharples, J. (2013). The physical oceanography of Jones Bank: A mixing hotspot in the Celtic Sea. *Progress in Oceanography*, *117*, 9–24. https://doi.org/10.1016/j.pocean.2013.06.009

Pandey, A. C., & Rai, S. (2008). Sensitivity of the Indian Ocean circulation to surface wind stress. http://nopr.niscair.res.in/handle/123456789/488

Popova, E., Yool, A., Byfield, V., Cochrane, K., Coward, A. C., Salim, S. S., et al. (2016). From global to regional and back again: Common climate stressors of marine ecosystems relevant for adaptation across five ocean warming hotspots. *Global Change Biology*, *22*(6), 2038–2053. https://doi.org/10.1111/gcb.13247

Pujol, M. I., Faugère, Y., Taburet, G., Dupuy, S., Pelloquin, C., Ablain, M., & Picot, N. (2016). DUACS DT2014: The new multi-mission altimeter data set reprocessed over 20 years. *Ocean Science*, *12*(5), 1067–1090.

Racault, M. F., Sathyendranath, S., Brewin, R. J., Raitsos, D. E., Jackson, T., & Platt, T. (2017). Impact of El Niño variability on oceanic phytoplankton. *Frontiers in Marine Science*, *4*, 133. https://doi.org/10.3389/fmars.2017.00133

Raitsos, D. E., Pradhan, Y., Brewin, R. J., Stenchikov, G., & Hoteit, I. (2013). Remote sensing the phytoplankton seasonal succession of the Red Sea. *PLoS ONE*, *8*(6), e64909. https://doi.org/10.1371/journal.pone.0064909

Richardson, P., & McKee, T. (1989). Surface velocity in the equatorial oceans calculated from historical ship drifts. WHOI Technological Report. WHOI-89-9, 50 pp. [Available from WHOI, Woods Hole, MA 02543.]

Roberts, M. J., Ribbink, A. J., Morris, T., Duncan, F., Barlow, R., Kaehler, S., et al. (2008). *2007 Western Indian Ocean Cruise and Data Report Alg 160*. Grahamstown: African Coelacanth Ecosystem Programme.

Robinson, J., New, A. L., Popova, E. E., Srokosz, M. A., & Yool, A. (2017). Far-field connectivity of the UK's four largest marine protected areas: Four of a kind? *Earth's Future*, *5*, 475–494. https://doi.org/10.1002/2016EF000516

Robinson, J. O. S. I. E., Popova, E. E., Srokosz, M. A., & Yool, A. (2016). A tale of three islands: Downstream natural iron fertilization in the Southern Ocean. *Journal of Geophysical Research: Oceans*, *121*, 3350–3371. https://doi.org/10.1002/2015JC011319

Saji, N. H., Goswami, B. N., Vinayachandran, P. N., & Yamagata, T. (1999). A dipole mode in the tropical Indian Ocean. *Nature*, *401*(6751), 360. https://doi.org/10.1038/43854

Sanders, M. J., Sparre, P., & Venema, S. C. (1988). Proceedings on the Workshop on the Assessment of the Fishery Resources in the Southwest Indian Ocean. In *Workshop on the Assessment of the Fishery Resources in the Southwest Indian Ocean, Albion (Mauritius), 14-25 Sep 1987*.

Schott, F. A., Dengler, M., & Schoenefeldt, R. (2002). The shallow overturning circulation of the Indian Ocean. *Progress in Oceanography*, *53*(1), 57–103. https://doi.org/10.1016/S0079-6611(02)00039-3

Schott, F. A., & McCreary, J. P. Jr. (2001). The monsoon circulation of the Indian Ocean. *Progress in Oceanography*, *51*(1), 1–123. https://doi.org/10.1016/S0079-6611(01)00083-0

Schott, F. A., Xie, S. P., & McCreary, J. P. Jr. (2009). Indian Ocean circulation and climate variability. *Reviews of Geophysics*, *47*, RG1002. https://doi.org/10.1029/2007RG000245

Shenoi, S. S. C., Saji, P. K., & Almeida, A. M. (1999). Near-surface circulation and kinetic energy in the tropical Indian Ocean derived from Lagrangian drifters. *Journal of Marine Research*, *57*(6), 885–907. https://doi.org/10.1357/002224099321514088

Smith, S. L. (1982). The northwestern Indian Ocean during the monsoons of 1979: Distribution, abundance and feeding of zooplankton. *Deep Sea Research*, *29*, 1331–1353. https://doi.org/10.1016/0198-0149(82)90012-7

Song, Q., Gordon, A. L., & Visbeck, M. (2004). Spreading of the Indonesian throughflow in the Indian Ocean. *Journal of Physical Oceanography*, *34*(4), 772–792. https://doi.org/10.1175/1520-0485(2004)034<0772:SOTITI>2.0.CO;2

Srokosz, M. A., Robinson, J., McGrain, H., Popova, E. E., & Yool, A. (2015). Could the Madagascar bloom be fertilized by Madagascan iron? *Journal of Geophysical Research: Oceans*, *120*, 5790–5803.

Swallow, J. C., Schott, F., & Fieux, M. (1991). Structure and transport of the East African coastal current. *Journal of Geophysical Research*, *96*(C12), 22,245–22,257. https://doi.org/10.1029/91JC01942

Tamooh, F., Van den Meersche, K., Meysman, F., Marwick, T. R., Borges, A. V., Merckx, R., et al. (2012). Distribution and origin of suspended matter and organic carbon pools in the Tana River Basin, Kenya. *Biogeosciences*, *9*(8), 2905–2920. https://doi.org/10.5194/bg-9-2905-2012

Tilstone, G. H., Angel-Benavides, I. M., Pradhan, Y., Shutler, J. D., Groom, S., & Sathyendranath, S. (2011). An assessment of chlorophyll-*a* algorithms available for SeaWiFS in coastal and open areas of the Bay of Bengal and Arabian Sea. *Remote Sensing of Environment*, *115*(9), 2277–2291. https://doi.org/10.1016/j.rse.2011.04.028

Timmermann, R., Goosse, H., Madec, G., Fichefet, T., Ethe, C., & Duliere, V. (2005). On the representation of high latitude processes in the ORCA-LIM global coupled sea ice–ocean model. *Ocean Modelling*, *8*(1-2), 175–201. https://doi.org/10.1016/j.ocemod.2003.12.009

Tweddle, J. F., Sharples, J., Palmer, M. R., Davidson, K., & McNeill, S. (2013). Enhanced nutrient fluxes at the shelf sea seasonal thermocline caused by stratified flow over a bank. *Progress in Oceanography*, *117*, 37–47. https://doi.org/10.1016/j.pocean.2013.06.018

US Department of Commerce, National Oceanic and Atmospheric Administration, National Geophysical Data Center. (2006). 2-minute gridded global relief data (ETOPO2v2).

Varela, R., Álvarez, I., Santos, F., DeCastro, M., & Gómez-Gesteira, M. (2015). Has upwelling strengthened along worldwide coasts over 1982–2010? *Scientific Reports*, *5*, 10016. https://doi.org/10.1038/srep10016

Webber, B. G., Matthews, A. J., Vinayachandran, P. N., Neema, C. P., Sanchez-Franks, A., Vijith, V., et al. (2018). The dynamics of the Southwest Monsoon current in 2016 from high-resolution in situ observations and models. *Journal of Physical Oceanography*, *48*(10), 2259–2282. https://doi.org/10.1175/JPO-D-17-0215.1

Webster, P. J., Moore, A. M., Loschnigg, J. P., & Leben, R. R. (1999). Coupled ocean–atmosphere dynamics in the Indian Ocean during 1997–98. *Nature*, *401*(6751), 356. https://doi.org/10.1038/43848

Wickstead, J. (1961). Plankton on the North Kenya Banks. *Nature*, *192*, 890–891. https://doi.org/10.1038/192890a0

Wiggert, J. D., Vialard, J., & Behrenfeld, M. J. (2009). Basinwide modification of dynamical and biogeochemical processes by the positive phase of the Indian Ocean Dipole during the SeaWiFS era. In *Indian Ocean biogeochemical processes and ecological variability* (Vol. 185, pp. 385–407). Washington, DC: American Geophysical Union. https://doi.org/10.1029/2008GM000776

Williams, F. (1963). Longline fishing for tuna off the coast of east Africa 1958–1960. *Indian Journal of Fisheries*, *10*, 233–290.

Woodberry, K. E., Luther, M. E., & O'Brien, J. J. (1989). The wind-driven seasonal circulation in the southern tropical Indian Ocean. *Journal of Geophysical Research*, *94*(C12), 17,985–18,002. https://doi.org/10.1029/JC094iC12p17985

Yool, A., Popova, E. E., & Anderson, T. R. (2013). MEDUSA-2.0: an intermediate complexity biogeochemical model of the marine carbon cycle for climate change and ocean acidification studies. *Geoscientific Model Development*, *6*(5), 1767–1811. https://doi.org/10.5194/gmd-6-1767-2013

Zavala-Garay, J., Theiss, J., Moulton, M., Walsh, C., van Woesik, R., Mayorga-Adame, C. G., et al. (2015). On the dynamics of the Zanzibar Channel. *Journal of Geophysical Research: Oceans*, *120*, 6091–6113. https://doi.org/10.1002/2015JC010879

Zhang, R. H., Zebiak, S. E., Kleeman, R., & Keenlyside, N. (2005). Retrospective El Niño forecasts using an improved intermediate coupled model. *Monthly Weather Review*, *133*(9), 2777–2802. https://doi.org/10.1175/MWR3000.1